Check for updates



LASER & PHOTONICS REVIEWS
www.lpr-journal.org

# High-Speed High-Resolution Transport of Intensity Diffraction Tomography with Bi-Plane Parallel Detection

*Ning Zhou, Runnan Zhang, Weisheng Xu, Ruizhi Zhu, Hanci Tang, Xiao Zhou, Jiasong Sun, Peng Gao,* Qian Chen,* and Chao Zuo**

**A novel high-speed, high-resolution 3D microscopy technique named BP-TIDT is presented that quantifies the refractive index (RI) distribution of label-free, transparent samples. This method combines a bi-plane detection scheme (BP) with the transport of intensity diffraction tomography (TIDT), effectively circumventing the need for matched illumination conditions under high numerical aperture (NA) objectives, which enables 15 fps volume rates and 326 nm lateral resolution. The effectiveness and accuracy of the proposed approach are validated through high-resolution imaging of polystyrene microspheres and HepG2 cells. Moreover, the wide-ranging applicability of BP-TIDT is demonstrated by investigating subcellular organelle motion, including mitochondria and lipid droplets, as well as the macroscopic apoptosis process in living COS-7 cells. To the best of current knowledge, this is the first time that high spatial-temporal resolution dynamic ODT results are obtained in a non-interferometric and motion-free manner, highlighting the potential of BP-TIDT in advancing research on dynamic cellular processes.**

## 1. Introduction

Optical diffraction tomography (ODT) is an emerging 3D microscopy technique that enables label-free imaging of transparent biological samples by utilizing their intrinsic refractive index (RI) as a natural contrast mechanism. It offers the ability to visualize and quantitatively characterize the internal structures of such samples in 3D.[1–3] Unlike conventional fluorescence imaging methods, ODT eliminates the need for exogenous fluorescent dyes, avoiding potential issues such as phototoxicity and photobleaching.[4] As a result, this non-invasive and label-free approach has found widespread applications in various fields, including biophysics, cell biology, hematology, microbiology, and neuroscience, providing researchers with a powerful tool for biomedical research and clinical applications.[5–9]

Over the past few decades, researchers have developed different variants of ODT techniques by combining principles of holography and computer tomography.[10] These coherent ODT technologies, whether based on object rotation[8,11] or illumination scanning,[12,13] rely on coherent synthetic apertures to capture the necessary information.[14] Non-interferometric ODT based on asymmetric illumination only requires capturing 2D intensity images at different conditions using the relative angle changes between the sample and the illumination beam. These images are subsequently used to reconstruct the 3D RI of the specimen.[15,16] Thus, it has a unique advantage in efficient, dynamic 3D diffraction tomography.[17] However, conventional imaging devices only record the intensity or amplitude of light, resulting in the loss of valuable phase information that encodes the structural and optical properties of transparent specimens. Only when the numerical aperture (NA) of the illumination matches that of the objective lens, the two anti-symmetric apertures of the 2D phase transfer function (PTF) will displace and tangent each other, allowing the low-frequency phase information to be accurately transferred to the intensity image through non-interferometric measurements.[18] This phenomenon also affects ODT imaging.

In response to the above mentioned issues, our previous work captured axial intensity stacks from different illumination angles, extending the intensity transport from "2D planar transport" to

N. Zhou, R. Zhang, W. Xu, R. Zhu, H. Tang, X. Zhou, J. Sun, C. Zuo
Smart Computational Imaging Laboratory (SCILab)
School of Electronic and Optical Engineering
Nanjing University of Science and Technology
Nanjing, Jiangsu 210094, China
E-mail: zuochao@njust.edu.cn

N. Zhou, R. Zhang, W. Xu, R. Zhu, H. Tang, X. Zhou, J. Sun, Q. Chen, C. Zuo
Jiangsu Key Laboratory of Spectral Imaging & Intelligent Sense
Nanjing University of Science and Technology
Nanjing, Jiangsu 210094, China
E-mail: chenqian@njust.edu.cn

N. Zhou, R. Zhang, W. Xu, R. Zhu, H. Tang, X. Zhou, J. Sun, Q. Chen, C. Zuo
Smart Computational Imaging Research Institute (SCIRI) of Nanjing University of Science and Technology
Nanjing, Jiangsu 210094, China

P. Gao
School of Physics
Xidian University
Xi'an 710126, China
E-mail: peng.gao@xidian.edu.cn

The ORCID identification number(s) for the author(s) of this article can be found under https://doi.org/10.1002/lpor.202400387

**DOI: 10.1002/lpor.202400387**

 © 2024 Wiley-VCH GmbH

"3D volumetric transport".[19] The derived transfer function theory of 3D image formation showcases that the conjugated terms in the logarithmic intensity spectrum can always be separable in the 3D Fourier space, eliminating the requirement for matching illumination conditions in ODT imaging. However, this method requires extensive $z$-axis scanning, significantly compromising its temporal resolution. Zhou et al.[20] further reduced the axial defocus to two images, directly compensating for the low-frequency PTF by restoring the phase through the transport of intensity equation (TIE) method.[21] However, this method still has two drawbacks: 1) The low-frequency filling is still based on axial acquisition, requiring the imaging system to introduce mechanical motion (move twice); 2) It is still based on the iterative method of FPDT, which requires many iterations to converge.[15,22] Therefore, the TI-FPDT method cannot achieve high-speed ODT imaging, limiting its applicability in dynamic imaging of biological samples (such as living cells). So far, obtaining high spatial-temporal resolution dynamic 3D RI reconstructions in label-free non-interferometric ODT is a significant challenge.

To achieve axial image acquisition without compromising speed or sensitivity, researchers proposed several approaches to attain multi-plane detection without mechanical displacement.[23,24] By integrating an electrically tunable lens into a conventional microscope equipped with modified illumination, Zhang et al.[25] achieve real-time, motion-free, high spatial resolution all-in-focus imaging of thick specimens. Gao et al.[26,27] used an optical configuration for parallel two-step phase-shifting digital holographic microscopy (DHM) and suppressed the DC term by subtracting the two phase-shifting holograms from each other for real-time phase microscopy. Zuo et al.[28] achieved parallel acquisition of two axial planes using a phase-only spatial light modulators (SLM) module resembling a Michelson structure, and then reconstructed phase information by integrating this approach with the TIE method. This technique offers the benefits of instantaneous acquisition and adaptable defocus distance adjustment. However, these methods are all applied in the field of QPI imaging. To our knowledge, solving the axial acquisition problem through channel multiplexing in the field of ODT has not been reported.

In this work, we specifically integrated our previous work into the ODT method to address the abovementioned challenges. The rationale here is twofold: 1) Based on the TI-FPDT concept, two defocused images are sufficient to address the low-frequency transfer function missing problems caused by mismatched illumination under high NA conditions. Therefore, we only need to consider the parallel detection of two focal planes further. 2) In response to the iterative computation take-up time problem of FPDT, we derived a bi-plane TIDT theoretical model, directly solving the linear problem through a single deconvolution to obtain the 3D RI results of the sample. In summary, we proposed a new non-interferometric ODT system called transport of intensity diffraction tomography with bi-plane parallel detection (BP-TIDT) for high-speed, high-resolution 3D RI reconstruction. We constructed a microscopy imaging system based on a commercial microscope platform, incorporating LED illumination control and SLM aperture plane phase modulation. With a high NA objective lens (40×, 0.95 NA) and 0.65 NA illumination, we successfully achieved a high-resolution reconstruction of non-interferometric 3D RI with a resolution of 326 nm. Simulation and experimental results using polystyrene microspheres demonstrated the consistency and effectiveness of our BP-TIDT method in recovering low-frequency components under high NA conditions. Furthermore, we showed the capability of BP-TIDT in imaging biological samples through high-resolution RI tomography and quantitative characterization of unstained HepG2 cells. Finally, we showcased the high-speed 15 fps dynamic time-lapse 3D imaging of COS-7 cells in vitro. Both theoretical assessments and experimental results suggest that BP-TIDT holds promise as a valuable 3D imaging tool, suitable for a range of applications in biomedical and life sciences.

## 2. Principle

### 2.1. Experimental Setup

**Figure 1a** depicts the experimental setup of the BP-TIDT system. This setup leverages the benefits of non-interferometric detection, enabling straightforward integration with a standard inverted microscope (IX71, Olympus, Japan). The microscope is equipped with a 40×/0.95 NA objective lens (UPLXAPO40X, Olympus) and a high-speed quantitative CMOS camera (HAMAMATSU C15550-20UP, 4096×2304, 4.6 μm pixel pitch, 120 frames/s under CoaXPress). In addition, the illumination module comprises an annular LED (containing 24 surface-mounted LEDs, Adafruit) with a diameter of 112 mm as the source. Positioned 50 mm from the sample, this module facilitates multi-angle illumination with a peak NA of 0.65, ensuring the center of the illumination aligns with the microscope's optical axis. Each LED (WS2812B, SMD-5050) operates at approximately 200 mW, delivering spatially coherent and quasi-monochromatic illumination with a wavelength of 523 nm and a FWHM width of 26 nm. The ARM board controller (MIMXRT1062, ARM Cortex-M7 with a core clock speed of 600 MHz, Teensy 4.1, NXP Semiconductors) manages the sequential activation of the LED elements. Then, it passes through the sample, objective, and tube lens to generate an enlarged sample image at the camera output port (image plane).

In the configuration of the microscope's image plane, a pair of lenses, designated as $L_1$ and $L_2$, both with an equal focal length of 150 mm ($f = f_1 = f_2 = 150$mm), are aligned to form a telecentric $4f$ optical system. Within this system, a non-polarizing beam-splitter cube (BS) is employed to divide the incoming beam into two distinct beams: one of reflection and one of transmission. These two beams are then directed toward their respective Fourier planes: namely, a spatial light modulator (SLM) and a mirror (M). The SLM is configured with a reflective liquid crystal phase-only panel (Holoeye Pluto, 1920×1080 pixels, 8 μm pixel size) to provide full $2\pi$ phase modulation with linear electro-optic characteristics. More descriptions of the SLM can be found in Section S6 (Supporting Information). As depicted in Figure 1b, the setup facilitates the lateral separation and simultaneous capture of two distinct intensity images, each corresponding to a different defocus distance, directly onto the camera's focal plane. The mirror M and the SLM are tilted to form small angles with the optical axis, where the angles $\alpha \approx 2°$, resulting in a lateral displacement of the two reflected beams. Consequently, the two reflected beams experience a lateral offset of $\pm\alpha$. Upon traversing lens $L_2$, the angular misalignment of $2\alpha$ is translated into


© 2024 Wiley-VCH GmbH

18638899, 0, Downloaded from https://onlinelibrary.wiley.com/doi/10.1002/lpor.202400387 by Nanjing University Of Science, Wiley Online Library on [01/07/2024]. See the Terms and Conditions (https://onlinelibrary.wiley.com/terms-and-conditions) on Wiley Online Library for rules of use; OA articles are governed by the applicable Creative Commons License

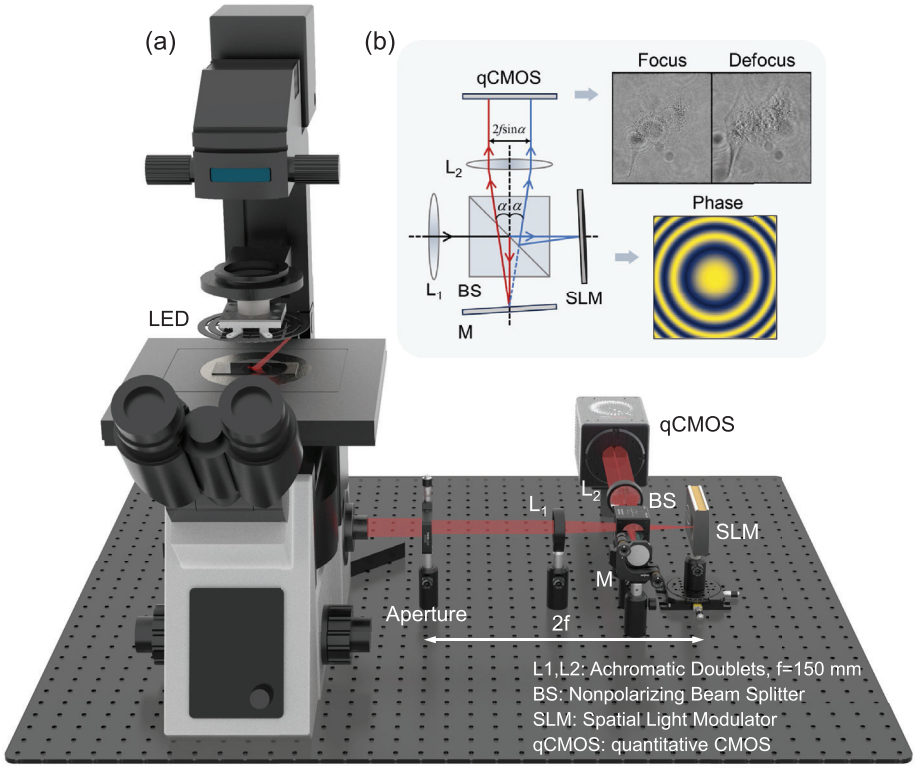


**Figure 1.** Experimental setup. BS: Non polarized beam splitter; L1, L2: lenses; M: reflector mirror; SLM: Spatial light modulator; More details about the imaging system and the imaging acquisition procedure are illustrated in Video S3 (Supporting Information).

a linear separation of $2f\sin\alpha$ along the image's width, effectively dividing the image into two halves. To prevent the two images from overlapping and to optimize the camera sensor's active area, a rectangular aperture is strategically placed behind the microscope's imaging plane to perform plane filtering. A quadratic phase pattern, representative of the free-space transfer function, is projected onto the SLM, facilitating further axial focusing displacement of the transmitted beam along the $\Delta z$ axis. The capability of the SLM to "digitally defocus" the wavefront has been successfully showcased at macroscopic scales and is utilized in the context of smooth wavefront sensing.[29,30] Before the SLM, a linear polarizer is installed to enhance phase modulation efficiency, while a neutral density filter ensures equal average intensities are distributed to the camera's left and right sides (components not depicted in Figure 1 for clarity).[28] The ARM controller orchestrates synchronization between the annular LED and the camera. This is achieved by triggering and monitoring the exposure status via a pair of coaxial cables, which allows for the simultaneous acquisition of bi-plane intensity dataset at a rate of 120 Hz from the camera. Subsequently, the BP-TIDT algorithm, as proposed, is utilized to reconstruct the 3D RI distribution of the sample under high NA and unmatched illumination conditions.

### 2.2. BP-TIDT Forward Imaging Model

Assuming a unit-amplitude quasi-monochromatic plane wave illuminates the sample, it can be considered that the total field $U(\mathbf{r})$ is the coherent superposition of the incident field $U_{in}(\mathbf{r})$ and the scattered field $U_s(\mathbf{r})$, *i.e.*, $U(\mathbf{r}) = U_{in}(\mathbf{r}) + U_s(\mathbf{r})$.[15] It should be noted that we do not explicitly differentiate spatial dimensions in this paper, where the variable $\mathbf{r} = (x, y)$ denotes the 2D spatial coordinates in the scene of 2D QPI and the $\mathbf{r} = (x, y, z) = (\mathbf{r}_T, z)$ denotes 3D spatial coordinates in the scene of 3D ODT, with $\mathbf{r}_T$ denoting the lateral spatial coordinate. For the viability in multiple scenarios, the contribution of the target is represented as a complex phase function $\varphi_s(\mathbf{r})$, given by:[19]

$$\begin{aligned}\varphi_s(\mathbf{r}) &= \ln\left[U(\mathbf{r})/U_{in}(\mathbf{r})\right] = \ln\left[1 + U_s(\mathbf{r})/U_{in}(\mathbf{r})\right] \\ &\equiv a(\mathbf{r}) + j\phi(\mathbf{r})\end{aligned} \tag{1}$$

Note that the form of Equation (1) is suitable for both 2D and 3D scenes. Based on the derivations presented in Section S3 (Supporting Information), within the framework of the first-order Born or Rytov approximation, the logarithmic Fourier spectrum of the captured intensity image (or intensity stack in 3D scenes) can be formulated as follows:[25]

$$\hat{I}(\mathbf{u}) = \hat{a}(\mathbf{u})H_a(\mathbf{u}) + \hat{\phi}(\mathbf{u})H_p(\mathbf{u}) \tag{2}$$

where $\hat{I}(\mathbf{u})$, $\hat{a}(\mathbf{u})$, $\hat{\phi}(\mathbf{u})$ and $\hat{\phi}(\mathbf{u})$ are the frequency domain representations of the field $I(\mathbf{r})$, the absorption component of the object $a(\mathbf{r})$, and the phase component of the object $\phi(\mathbf{r})$, respectively. $H_a(\mathbf{u})$ and $H_p(\mathbf{u})$ denote the transfer functions of the absorption components and of the phase components, respectively.


© 2024 Wiley-VCH GmbH

18638899, 0, Downloaded from https://onlinelibrary.wiley.com/doi/10.1002/lpor.202400387 by Nanjing University Of Science, Wiley Online Library on [01/07/2024]. See the Terms and Conditions (https://onlinelibrary.wiley.com/terms-and-conditions) on Wiley Online Library for rules of use; OA articles are governed by the applicable Creative Commons License

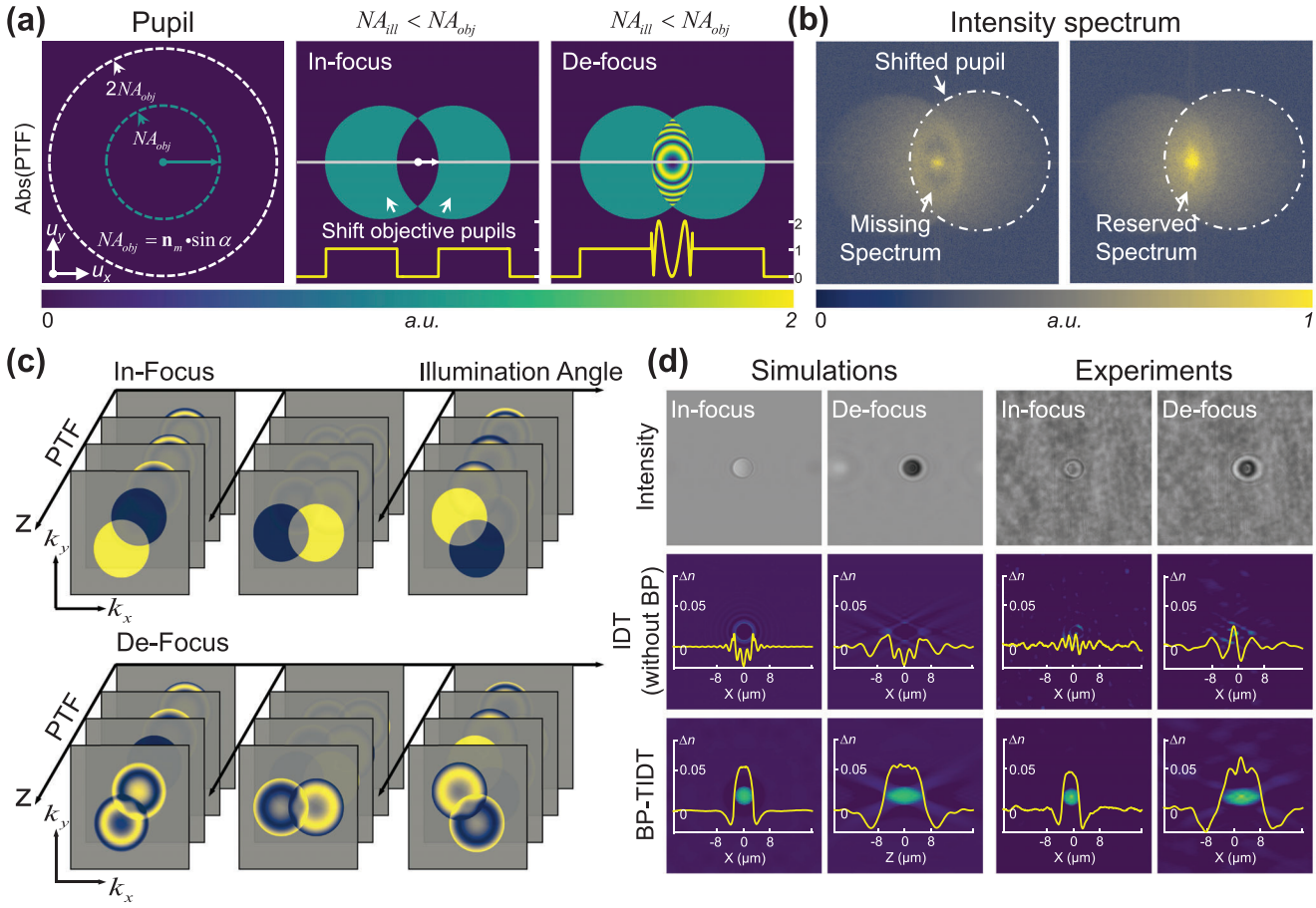


**Figure 2.** Illustrate the importance of illumination conditions and defocus phase modulation in non-interferometric ODT from the perspective of PTF and demonstrate the effectiveness of the BP-TIDT Method. a) Absolute value distribution of 2D PTF under different illumination conditions and defocus planes. b) Corresponding spectra of focused and defocused intensity images captured under unmatched illumination conditions. c) 5-D phase transfer functions under different illumination angles and defocus distances. d) Simulation and experimental results of polystyrene microspheres, including intensity images captured using bi-plane parallel detection and reconstruction results without and with using the BP-TIDT method.

For unlabeled transparent biological samples in 2D QPI and 3D ODT, the phase component $\Delta\phi$ is the primary determinant of the intensity contrast.[31] **Figure** 2a displays the 2D PTF of an imaging system free of aberration across various illumination configurations. It can be observed that an imaging system that is optimally focused and employs axial illumination ($U_{in} = 0$) fails to produce phase contrast due to two asymmetrical pupils negating each other's effects, which indicates why we can hardly observe the structure of the pure-phase object. However, increasing the illumination angle ($0 < |U_{in}| < NA_{obj}/\lambda$), can enable the separation of the pupils, preventing them from overlapping completely and making the phase information of the non-overlapping region visible. Nevertheless, the phase component in the low-frequency region (close to zero frequency) can be fully transferred to the intensity image only when the angle of illumination aligns with the NA of the objective lens ($|U_{in}| = NA_{obj}/\lambda$). The phenomenon of missing low-frequency phase components in the captured original intensity image at the focal plane is illustrated in Figure 2b, which further verifies this issue. This matching illumination condition is crucial for accurate phase recovery in non-interferometric QPI methods based on asymmetric illumination. However, it is challenging for high NA objectives to achieve matched illumination.

Besides modulation of the illumination angle, we can also introduce the phase part through defocus modulation in the transfer function to achieve the goal of encoding the phase information into the intensity image.[32] The absolute distribution of the defocused PTF in Figure 2a indicates that $H_p(\mathbf{u}_T; z = \Delta z)$ is always non-zero in the shifted pupil function. As depicted in Figure 2b, it implies that the phase components, particularly those in the lower frequency range, are capable of being completely transferred to the intensity image. The absolute value of the phase contrast in the non-overlapping region remains unchanged compared to the focused case, indicating that defocus is an energy transfer process.

The 3D PTF in Equation (2) can be written in the following form:

$$H_p(\mathbf{u}) = \frac{ik_0^2}{16\pi^3}\left\{ P(\mathbf{u}-\mathbf{u}_{in})\frac{\exp\left\{-i\left[\eta(\mathbf{u}-\mathbf{u}_{in})-\eta(\mathbf{u}_{in})\right](z+\Delta d)\right\}}{\eta(\mathbf{u}-\mathbf{u}_{in})} - P(\mathbf{u}+\mathbf{u}_{in})\frac{\exp\left\{i\left[\eta(\mathbf{u}+\mathbf{u}_{in})-\eta(\mathbf{u}_{in})\right](z+\Delta d)\right\}}{\eta(\mathbf{u}+\mathbf{u}_{in})}\right\} \quad (3)$$


© 2024 Wiley-VCH GmbH

18638899, 0, Downloaded from https://onlinelibrary.wiley.com/doi/10.1002/lpor.202400387 by Nanjing University Of Science, Wiley Online Library on [01/07/2024]. See the Terms and Conditions (https://onlinelibrary.wiley.com/terms-and-conditions) on Wiley Online Library for rules of use; OA articles are governed by the applicable Creative Commons License

where $\mathbf{u} = (k_x, k_y, z)$ denotes the frequency domain coordinates, $(k_x, k_y)$ represents the frequency coordinates, $\mathbf{u}_{in} = (k_{xi}, k_{yi})$ represents the spatial frequency of the incident field, $\eta(\mathbf{u}) = \sqrt{k_0^2 - |\mathbf{u}|^2}$ represents the axial wave vector, and $\Delta d$ represents the axial defocus distance of the sample. $P(\mathbf{u})$ is an ideal low pass filter with the cut-off frequency of $NA_{obj}/\lambda$, presents the pupil function of the objective lens.[18] By discretizing the 3D sample along the $z$-axis, the axial position is represented as $z = m\Delta z$, where $\Delta z$ is the axial sampling interval (*i.e.*, the spacing between slices), and $m$ is the index of the $M$ slices distributed along the $z$-axis. The detailed derivation process of the Equation (3) is provided in Section S4.2 (Supporting Information). In the context of 3D tomographic imaging, it is important to recognize that the traditional distinction between the focal plane and various defocus planes is not as rigid. This is because, in tomographic reconstruction, information from both the nominal in-focus and nominal out-of-focus planes contributes to the overall 3D image.[33] For the sake of convenience in our representation, we designate the central layer of the sample as the focal plane and consider all other planes to be defocused. Thus, as shown in Figure 2c, the transfer function corresponding to the bi-plane parallel measurement can be represented as:

$$H_p = \begin{cases} H_p(k_x, k_y, z, l, \Delta d = 0) & \text{in} - \text{focus} \\ H_p(k_x, k_y, z, l, \Delta d = d) & \text{de} - \text{focus} \end{cases} \tag{4}$$

where $l \rightarrow \mathbf{u}_{in} = (k_{xi}, k_{yi})$ represents the $l^{\text{th}}$ intensity image acquired under the illumination angle. Therefore, the intensity images obtained from bi-plane measurements can fully capture the phase components of different layers in the sample scattering potential. By combining angle-scanning illumination and bi-plane parallel measurements, BP-TIDT allows for the recovery of RI at arbitrary illumination angles ($0 < |U_{in}| < NA_{obj}/\lambda$) without suffering from low-frequency missing and degraded reconstruction quality.

### 2.3. BP-TIDT Reconstruction Algorithm

In the fundamental theory of ODT, the desired physical quantity to retrieve is the scattering potential $O(\mathbf{r}) = k_0^2\left[n(\mathbf{r})^2 - n_m^2\right]$ of a thick 3D sample, where $n(\mathbf{r})$ represents the complex RI distribution of the object, $k_0 = 2\pi/\lambda$ is the wave vector in free space, $\lambda$ is the illumination wavelength, and $n_m$ is the scattering potential of the surrounding medium. Assuming $\Delta\varepsilon(\mathbf{r}) = n(\mathbf{r}) - n_{\text{m}}$ stands for the dielectric constant of the sample, which represents local variations in RI, and $\Delta\varepsilon(\mathbf{r})$ is taken as smaller, we can express the complex scattering potential $O$ as:[34]

$$O(\mathbf{r}) = k_0^2\left[\Delta\varepsilon_{\text{Re}}(\mathbf{r}) + i\Delta\varepsilon_{Im}(\mathbf{r})\right] \tag{5}$$

The FT is performed along $x$ and $y$ at each given $z$ of the object yields $\widehat{O}\left(k_x, k_y, z\right) = k_0^2\left[\widehat{\Delta\varepsilon}_{\text{Re}}\left(k_x, k_y, z\right) + i\widehat{\Delta\varepsilon}_{Im}\left(k_x, k_y, z\right)\right]$. In the equation, $\Delta\varepsilon_{\text{Re}}$ represents the real part of $\Delta\varepsilon$, indicating the influence of phase on the object, while $\Delta\varepsilon_{Im}$ represents the imaginary part, which indicates the influence of absorption. In Section 2.2, we discussed the forward model for intensity formation. This section will focus on reconstructing the sample's RI and absorption from the measured intensity images in BP-TIDT.

First, the background is removed from each intensity image, as shown in Section S5 (Supporting Information) step 2. Next, based on the derived transfer function from the forward model, the interpolation between actual measured values and predicted measured values is minimized using the $l_2$-norm through a least squares algorithm.[35] It is worth noting that because of the limited angular coverage of illumination and imaging optics, "missing cones" exist along the axial dimension in both the phase and absorption transfer functions. Therefore, direct inversion would lead to high-frequency artifacts due to information loss.[36,37] This issue can be effectively mitigated by applying a least total energy constraint and Tikhonov regularization:

$$\min_{\widehat{\Delta\varepsilon}_{\text{Re}}, \widehat{\Delta\varepsilon}_{Im}} \sum_{l,\Delta d} \left\| \hat{I} - H_p\widehat{\Delta\varepsilon}_{\text{Re}} - H_a\widehat{\Delta\varepsilon}_{Im} \right\|_2^2 + \alpha\left\|\widehat{\Delta\varepsilon}_{\text{Re}}\right\|_2^2 + \beta\left\|\widehat{\Delta\varepsilon}_{Im}\right\|_2^2 \tag{6}$$

where $\|.\|_2^2$ represents the $l_2$-norm of a vector, $\alpha$ and $\beta$ are regularization parameters, $\hat{I}$ is the normalized Fourier transform of the collected intensity data, $H_p$ and $H_a$ are the transfer functions for phase and absorption, respectively, as derived from Section 2.2. Finally, setting the first derivatives of the equations to zero yields a closed-form solution:

$$\Delta\varepsilon_{\text{Re}} = \mathscr{F}^{-1}\left\{ \frac{-\sum_{l,\Delta d} H_p(l,\Delta d)\beta\hat{I}[l,\Delta d]}{\sum_{l,\Delta d}\left|H_a(l,\Delta d)\right|^2\alpha + \sum_{l,\Delta d}\left|H_p(l,\Delta d)\right|^2\beta + \alpha\beta} \right\} \tag{7}$$

$$\Delta\varepsilon_{Im} = \mathscr{F}^{-1}\left\{ \frac{-\sum_{l,\Delta d} H_a(l,\Delta d)\alpha\hat{I}[l,\Delta d]}{\sum_{l,\Delta d}\left|H_a(l,\Delta d)\right|^2\alpha + \sum_{l,\Delta d}\left|H_p(l,\Delta d)\right|^2\beta + \alpha\beta} \right\} \tag{8}$$

where $\mathscr{F}^{-1}$ represents the 2D inverse Fourier transform, $l$ represents the intensity image acquired under the $l^{\text{th}}$ illumination angle, $H_a$ and $H_p$ represent discrete absorption and phase 5-D transfer functions respectively, and $\hat{I}[l,\Delta d]$ is the Fourier spectrum of the intensity image after background subtraction. The detailed derivation of Equations can be found in Section S4.3 (Supporting Information). Then, based on the relationship between $n_{\text{Re}} = \sqrt{\left(\left(n_0^2 + \Delta\varepsilon_{\text{Re}}\right) + \sqrt{\left(n_0^2 + \Delta\varepsilon_{\text{Re}}\right)^2 + \Delta\varepsilon_{\text{Im}}^2}\right)/2}$ and $n_{\text{Im}} = \Delta\varepsilon_{\text{Im}}/2n_{\text{Re}}$,[31] the 3D RI distribution of the sample can be reconstructed. The detailed workflow of BP-TIDT for 3D RI reconstruction can be found in Section S5 (Supporting Information).

### 2.4. Validation of BP-TIDT

To validate the quantitative 3D RI reconstruction capability of our BP-TIDT system, we conducted experiments using polystyrene microspheres as test samples and compared the results with simulations of a pure phase microsphere. Both the experimental and


© 2024 Wiley-VCH GmbH

18638899, 0, Downloaded from https://onlinelibrary.wiley.com/doi/10.1002/lpor.202400387 by Nanjing University Of Science, Wiley Online Library on [01/07/2024]. See the Terms and Conditions (https://onlinelibrary.wiley.com/terms-and-conditions) on Wiley Online Library for rules of use; OA articles are governed by the applicable Creative Commons License

simulated reconstructions were performed with consistent parameters to ensure the validity of our comparative analysis. The ideal microsphere with a 6 μm diameter and RI of 1.60 was immersed in a matched medium ($n_m$ = 1.518, Olympus, Japan). Experimentally, the LEDs on the ring were sequentially illuminated, generating planar waves with a central wavelength of 523 nm and illumination $NA_{ill}$ = 0.65 from different angles, passing through the sample. Phase modulation patterns were generated on the back-end SLM to create axial "digital defocus" effect. The reflected beams in the 4$f$ system were laterally displaced by $\pm\alpha$ angles to spatially separate and synchronously capture intensity images with different defocus distances on the camera's focal plane. In Section S1 (Supporting Information), we analyzed the selection of defocus distance based on the PTF, and provided the optimal defocus distance suitable for our current system based on system's parameters. The first row of Figure 2d shows the intensity images captured in different focal planes during simulation and experiment, respectively. The combination of bi-plane parallel detection and illumination angle scanning resulted in 24 images.

Since the maximum 0.65 NA illumination was less than the 40× 0.95 NA objective, the traditional IDT method failed to recover the microsphere's RI correctly, only reconstructing sharp edges (high-frequency details), as shown in the second row of Figure 2d. This phenomenon is consistent with our prediction of low-frequency RI loss resulting from unmatched illumination conditions. With the bi-plane parallel detection, the additional defocused intensity images acquired at each illumination angle provided low-frequency phase contrast, enabling the proposed method to recover the microsphere's low-frequency RI. As shown in the third row of Figure 2d, the experimental results showed indistinguishable differences from the simulation results, indicating that the BP-TIDT technique can effectively achieve quantitative RI recovery without the need for additional axial mechanical displacement, overcoming the degradation in reconstruction quality and underestimation of RI observed in traditional IDT under non-matched illumination conditions.

## 3. Results

### 3.1. Tomographic Imaging of Unstained Hepg2 Cells

To demonstrate the biological applications of BP-TIDT, we first imaged unlabeled HepG2 cells and achieved high-resolution RI tomography. **Figure 3**a,b display the reconstructed RI results of two different subregions within a 40× field of view (FOV) using BP-TIDT, along with the reconstruction results using IDT as a control. The enlarged RI distributions and nucleoli contours corresponding to the rectangular subregions shown in Figure 3 c1–d2 highlight the differences in low-frequency components between the reconstruction results using the two different algorithms. The comparative results suggest that BP-TIDT overcomes the RI underestimation caused by unmatched illumination conditions and accurately recovers the RI of biological cells.

Figure 3e,f shows that the tomographic scans of two regions of interest (ROI) at different axial depths demonstrate high-resolution visualization of filamentous extensions and other subcellular features, including cell boundaries, nucleoli, and dark vesicles. Experimental results confirm that the traditional IDT method is limited by missing low-frequency information in complex biological samples under high NA objective lenses due to mismatched illumination conditions. The profiles in Figure 3g,h validate that while ensuring near-diffraction-limited lateral resolution of approximately 328 nm, the BP-TIDT method significantly enhances the low-frequency information in the reconstructed RI, resulting in more accurate cellular morphology.

### 3.2. Dynamic 3D RI Imaging of Live Cells

Finally, we applied the proposed BP-TIDT method to perform label-free time-lapse 3D imaging of live COS-7 cells. It should be noted that when measuring live samples, it is necessary to choose appropriate illumination schemes and exposure times to reduce motion-related artifacts. The qCMOS camera in this experiment provides extremely low readout noise of 0.27 electrons,[38] enhancing the signal-to-noise ratio in low-light imaging conditions. In Section S2 (Supporting Information), we analyzed the illumination scheme and found that at least eight original images can provide better data support for the solution. Therefore, each RI stack reconstruction utilized 8 frame images in the time-lapse sequence, these images were acquired with a 5 ms exposure interval. It was then separated into focused and defocused intensity image sets. This allowed us to break the matched illumination imaging conditions under a 0.95 NA objective lens and achieve an imaging speed of 15 fps for displacement-free high spatiotemporal resolution 3D RI imaging.

**Figure 4**a illustrates the RI slice of the entire field of view reconstructed at $z$ = 0 μm under a 40× 0.95 NA objective lens for COS-7 cells. We selected three ROIs and magnified these areas to highlight subcellular details and dynamics at different depths. ROI 1 shows $x-y$ slices at different axial depths at 00 : 00, demonstrating high-resolution visualization of mitochondria, cell boundaries, lipid droplets, and dark vesicles (indicated by arrows in ROI 1). The ROI2 region highlights the rapid transport of small black vesicles and lipid droplets within the cytoplasm (indicated by the circle in ROI2) and the nuclear membrane structures of two nucleoli (indicated by the arrow in ROI2). Furthermore, another subregion emphasizes the fast movement of mitochondria and the fish fin-like oscillation effect generated by the coordinated movement of cilia (indicated by the circle in ROI3), exhibiting high resolution and high RI contrast. Figure 4b illustrates the 3D volume rendering views of COS-7 cells reconstructed from four perspectives, visually illustrating the sample's 3D structure and distribution. It can be referred to Video S1 (Supporting Information) for more information on RI stack slices and corresponding temporal evolution videos of live COS-7 cells.

**Figure 5** further provides the dynamic apoptosis process 3D RI imaging results of other COS-7 cells. Mitochondria and lipid droplets are crucial organelles in cell energy production and storage, which regulate cellular metabolism energy balance and influence cell growth, division, and function. With enhanced spatiotemporal sensitivity, the BP-TIDT method enables the observation of intense movements of mitochondria and lipid droplet structures during the apoptosis process in COS-7 cells, as well as the interactions between these two organelles, as shown in Figure 5b–d. ROI2-ROI4 correspond to the magnified images of the regions enclosed by the white dashed boxes in b–d, where distinct subcellular particles with different RI values can


© 2024 Wiley-VCH GmbH

18638899, 0, Downloaded from https://onlinelibrary.wiley.com/doi/10.1002/lpor.202400387 by Nanjing University Of Science, Wiley Online Library on [01/07/2024]. See the Terms and Conditions (https://onlinelibrary.wiley.com/terms-and-conditions) on Wiley Online Library for rules of use; OA articles are governed by the applicable Creative Commons License

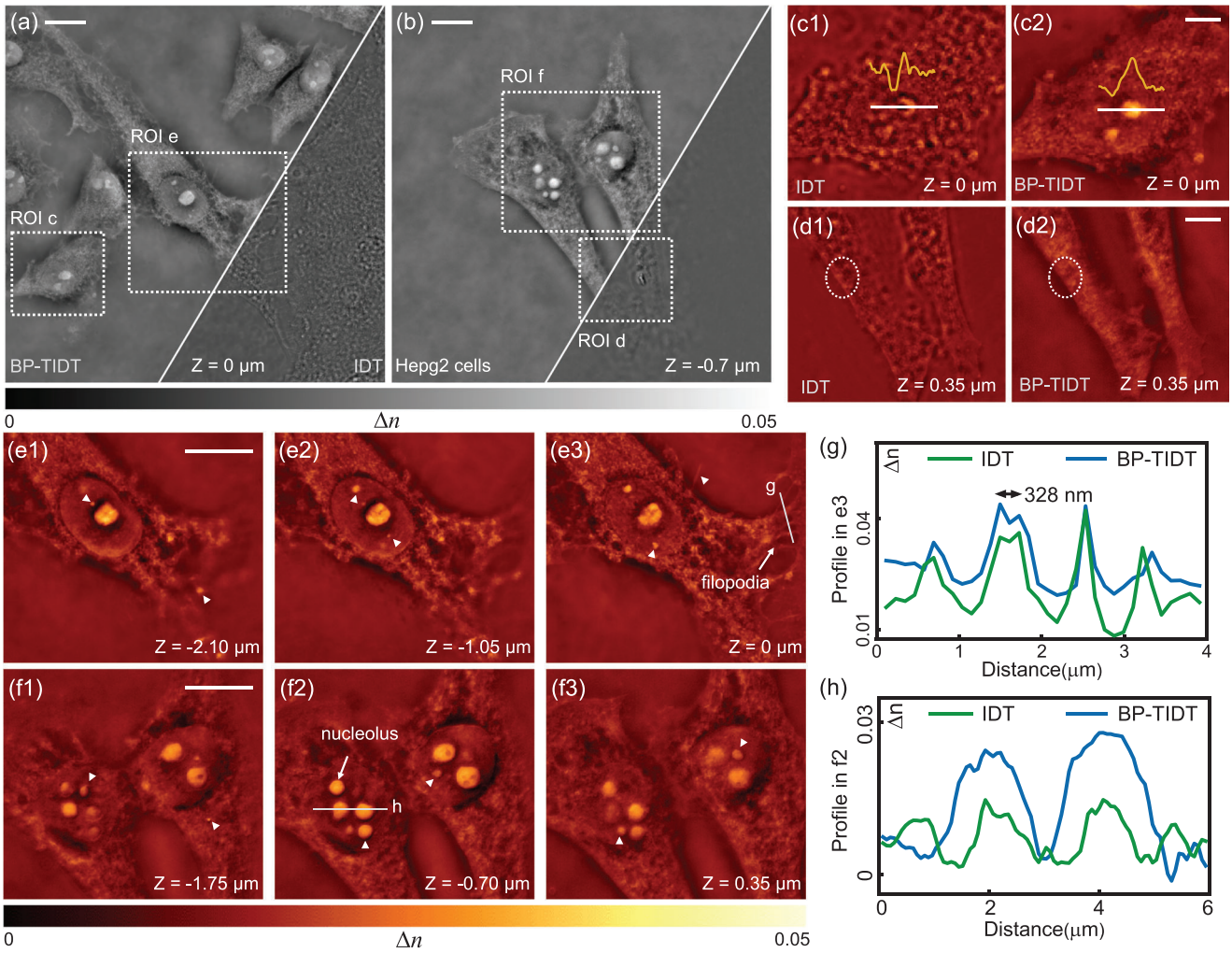


**Figure 3.** 3D RI reconstruction of unlabeled HepG2 cells under a 40X 0.95 NA objective lens. a,b) 3D RI reconstruction of two different subregions of HepG2 cells at 0 μm and -0.7 μm planes, respectively, within a 40X field of view using BP-TIDT and IDT. c1,c2,d1,d2) RI slices recovered by IDT and BP-TIDT corresponding to the rectangular subregions in (a) and (b). e,f) RI distribution of HepG2 cells at multiple z planes corresponding to the two square subregions in (a) and (b). g,h) RI profiles across subcellular structures quantifying the lateral resolution and RI values. Scale bar, (a,b,e,f) 5 μm; (c,d) 2 μm.

be observed, such as high-RI lipid droplets and low-RI black vesicles (indicated by white arrows). Moreover, at 14 min, the cells exhibited noticeable contraction, with the fin-like pseudopodia moving toward the center. The RI contrast increased significantly, but the overall morphology of the fin-like pseudopodia remained adhered to the glass substrate (indicated by circles in Figure 5c). In Video S2 (Supporting Information), we provide a dynamic apoptosis video of COS-7 cells, showcasing the movements of mitochondria, lipid droplets, and fin-like pseudopodia, visible on high-resolution RI slices with negligible motion blur over time. In Figure 5e–h, the line contours spanning these submicron-scale organelles exhibit a lateral resolution close to the diffraction limit of 326 nm. Furthermore, since the BP-TIDT method overcomes the issue of low-frequency loss in high-NA imaging, it allows high-NA objectives in application scenarios where illumination angles are limited, such as 96-well plate sample chambers. Therefore, the BP-TIDT method is particularly suitable for high-throughput/high-content imaging. In Section S7 (Supporting Information), we observed the division process of COS-7 living cells using a 96-well plate. Further dynamic results and detailed visualizations are provided in Video S4 (Supporting Information). These findings demonstrate the capability of BP-TIDT to observe unlabeled live cells in a conventional inverted microscope setup, allowing for long-duration, high-resolution, and high-contrast 3D microscopy imaging.

## 4. Discussion and Conclusion

To conclude, we proposed a novel BP-TIDT method and constructed a corresponding ODT experimental setup. By combining a bi-plane detection scheme with the transport of intensity diffraction tomography technology, this novel approach can effectively overcome the problems of reconstruction quality deterioration and RI underestimation of conventional non-interference ODT under non-matching illumination conditions without compromising speed and resolution. Through PTF


© 2024 Wiley-VCH GmbH

18638899, 0, Downloaded from https://onlinelibrary.wiley.com/doi/10.1002/lpor.202400387 by Nanjing University Of Science, Wiley Online Library on [01/07/2024]. See the Terms and Conditions (https://onlinelibrary.wiley.com/terms-and-conditions) on Wiley Online Library for rules of use; OA articles are governed by the applicable Creative Commons License

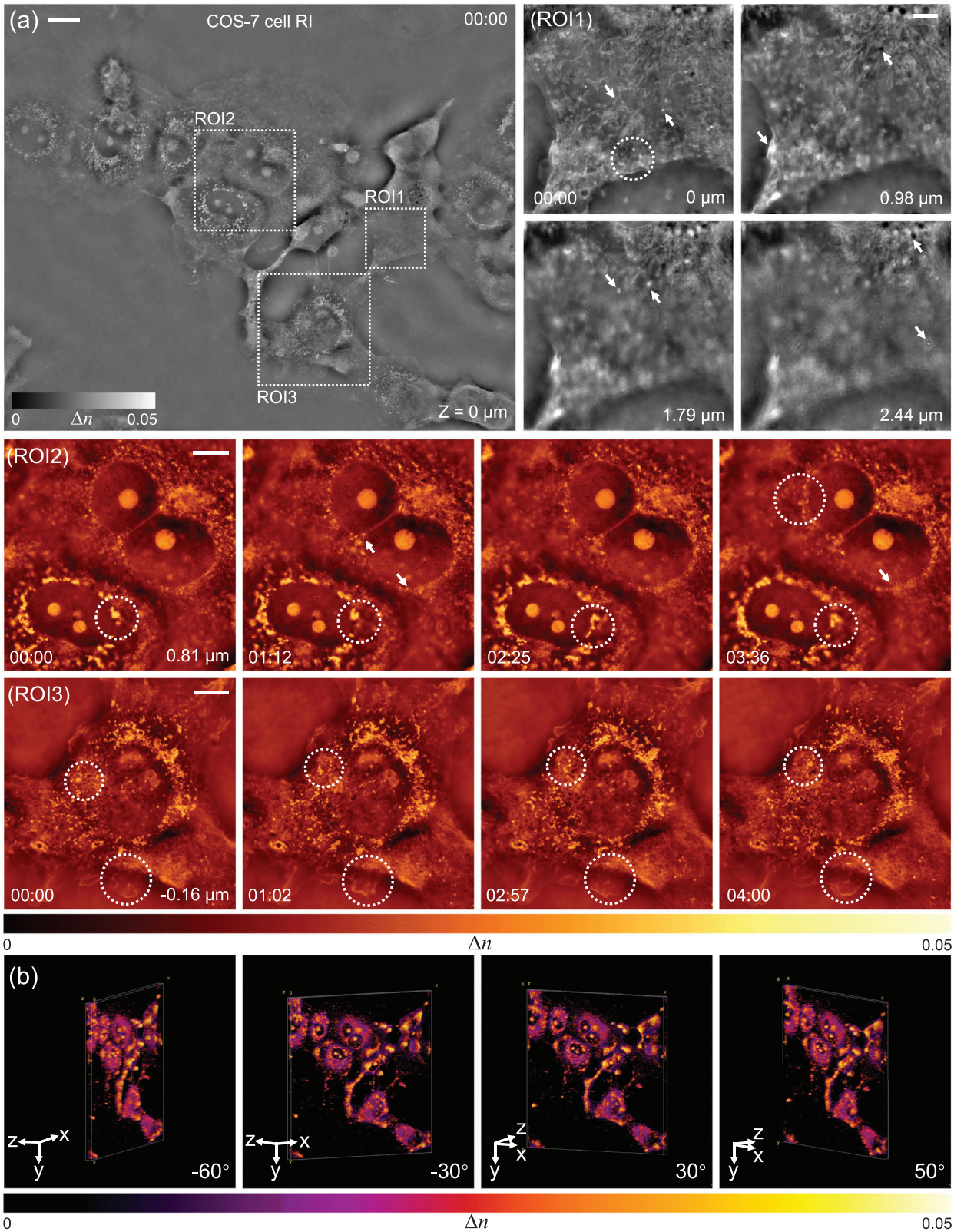


**Figure 4.** Time-lapse 3D RI imaging of COS-7 cells. a) Full-field RI slices of COS-7 cells located at the z = 0 μm plane are recovered at t=0 s, with three different ROI regions magnified within the field of view. The complete visualization process of the COS-7 cell is provided in Video S1 (Supporting Information). b). 3D volume renderings of COS-7 cells reconstructed at t=0 from different perspectives. Scale bar, (a) 20 μm; (ROI1) 5 μm; (ROI2) (ROI3) 10 μm.


© 2024 Wiley-VCH GmbH

18638899, 0, Downloaded from https://onlinelibrary.wiley.com/doi/10.1002/lpor.202400387 by Nanjing University Of Science, Wiley Online Library on [01/07/2024]. See the Terms and Conditions (https://onlinelibrary.wiley.com/terms-and-conditions) on Wiley Online Library for rules of use; OA articles are governed by the applicable Creative Commons License

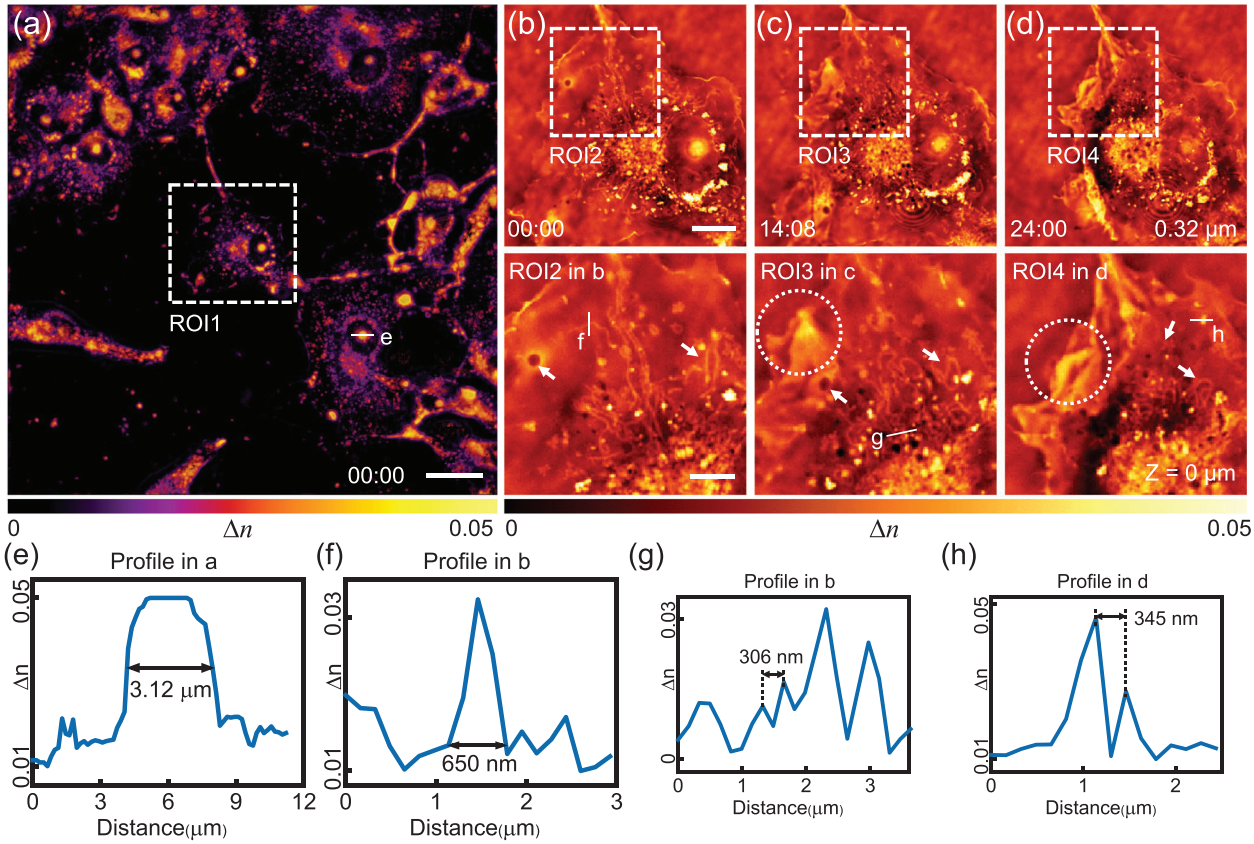


**Figure 5.** Label-free visualization of the complete apoptosis process of a COS-7 cell in three dimensions, in which various subcellular structures are observed. a) 3D RI rendering of COS-7 cells at 00:00. b–d) Magnified images of the regions enclosed by the white dashed box in (a) at three different time points, illustrating the entire process of cell apoptosis (see Video S2, Supporting Information). (ROI2)-(ROI4) correspond to the magnified images of the regions enclosed by the white dashed boxes in (b–d), showing smaller structures such as vesicles, mitochondria, lipid droplets (indicated by arrows), as well as the contraction of filopodia during the apoptosis process (indicated by dotted circles). (e–h) Line profiles across subcellular structures to quantify the reconstructed resolution. Scale bars: a) 30 μm; b–d) 10 μm; ROI2, ROI3, ROI4 5 μm.

analysis, we derived a bi-plane TIDT theoretical model, directly solving the linear problem through a single deconvolution to obtain the 3D RI results of the sample, which can solve the computational time consumption inherent in the traditional iterative solution method. Additionally, we analyzed the effects of the defocus distance and illumination scheme of BP-TIDT on imaging quality and speed. Reconstruction results on polystyrene microspheres, HepG2, and living COS-7 samples demonstrate that the proposed BP-TIDT enables 15 fps volume rates and 326 nm lateral resolution. As far as we are aware, this marks the initial instance of achieving high spatial-temporal resolution dynamic ODT outcomes without the use of interferometric or motion manner. This breakthrough underscores the promise of BP-TIDT as a leading non-invasive technique for probing the structure and dynamics of biological phenomena at cellular and subcellular scales.

Nonetheless, there are still several key issues that warrant further exploration or elucidation. The BP-TIDT tomographic method, which we proposed, frees itself from the need for matched illumination through defocus phase modulation. However, it continues to depend on the first-order Rytov approximation for its theoretical framework. The efficacy of this model is contingent upon the RI within the sample, which may restrict its use in samples that exhibit multi-layering or significant scattering.[39,40] Furthermore, because of the restricted range of incident beam angles, certain spatial frequency components along the light axis are unattainable, i.e., missing cone problem.[41] This issue not only degrades axial resolution but also impedes the precision of RI reconstruction and can introduce a halo effect at the periphery of cell imaging. This problem may be alleviated by incorporating previously proposed opposite illumination strategies in our future work.[42] Alternatively, the emerging field of learning-based 3D tomographic methods could be utilized to properly parameterize the missing cone artifacts and unknown experimental variables, such as optical aberrations and slight misalignments of the LEDs. This method could further optimize the imaging performance. Moreover, to gain additional biomolecular specificity, the integration of fluorescence super-resolution 3D technology such as confocal,[43] 3D-SIM[44] into BP-TIDT can be considered. A more expansive and profound understanding of biological processes can be unlocked by harnessing the precision of fluorescence methodologies in tandem with the non-invasive nature of diffraction tomography. This synergy paves the way for a more comprehensive exploration of cellular and subcellular dynamics, promising to significantly advance the field of biological imaging.[45,46]


© 2024 Wiley-VCH GmbH

18638899, 0, Downloaded from https://onlinelibrary.wiley.com/doi/10.1002/lpor.202400387 by Nanjing University Of Science, Wiley Online Library on [01/07/2024]. See the Terms and Conditions (https://onlinelibrary.wiley.com/terms-and-conditions) on Wiley Online Library for rules of use; OA articles are governed by the applicable Creative Commons License

## Supporting Information

Supporting Information is available from the Wiley Online Library or from the author.

## Acknowledgements

N.Z., R.Z., and W.X. contributed equally to this work. This work was supported by the National Natural Science Foundation of China (62227818, 62361136588, 62105151, 62175109, U21B2033), National Key Research and Development Program of China (2022YFA1205002), Leading Technology of Jiangsu Basic Research Plan (BK20192003), Youth Foundation of Jiangsu Province (BK20210338), Biomedical Competition Foundation of Jiangsu Province (BE2022847), Key National Industrial Technology Cooperation Foundation of Jiangsu Province (BZ2022039), Fundamental Research Funds for the Central Universities (30920032101, 30923010206), Fundamental Research Funds for the Central Universities (2023102001), and Open Research Fund of Jiangsu Key Laboratory of Spectral Imaging & Intelligent Sense (JSGP202105, JSGP202201).

## Conflict of Interest

The authors declare no conflict of interest.

## Data Availability Statement

The data that support the findings of this study are available from the corresponding author upon reasonable request.

## Keywords

3D microscopy, defying the matched illumination condition, optical diffraction tomography, transport-of-intensity

Received: March 20, 2024
Revised: June 4, 2024
Published online:

[1] E. Wolf, *Opt. Commun.* **1969**, *1*, 153.
[2] K. Lee, S. Shin, Z. Yaqoob, P. T. So, Y. Park, *J. Biophotonics* **2019**, *12*, 201800289.
[3] O. Haeberlé, K. Belkebir, H. Giovaninni, A. Sentenac, *J. Mod. Opt.* **2010**, *57*, 686.
[4] T. H. Nguyen, M. E. Kandel, M. Rubessa, M. B. Wheeler, G. Popescu, *Nat. Commun.* **2017**, *8*, 210.
[5] Y. Sung, W. Choi, C. Fang-Yen, K. Badizadegan, R. R. Dasari, M. S. Feld, *Opt. Express* **2009**, *17*, 266.
[6] Y. Park, C. Depeursinge, G. Popescu, *Nat. Photonics* **2018**, *12*, 578.
[7] T. A. Zangle, M. A. Teitell, *Nat. Methods* **2014**, *11*, 1221.
[8] F. Merola, P. Memmolo, L. Miccio, R. Savoia, M. Mugnano, A. Fontana, G. D'ippolito, A. Sardo, A. Iolascon, A. Gambale, P. Ferraro, *Light: Sci. Appl.* **2017**, *6*, e16241.
[9] Y. Shu, J. Sun, J. Lyu, Y. Fan, N. Zhou, R. Ye, G. Zheng, Q. Chen, C. Zuo, *PhotoniX* **2022**, *3*, 24.
[10] W. Choi, C. Fang-Yen, K. Badizadegan, S. Oh, N. Lue, R. R. Dasari, M. S. Feld, *Nat. Methods* **2007**, *4*, 717.
[11] M. Lee, K. Kim, J. Oh, Y. Park, *Light: Sci. Appl.* **2021**, *10*, 102.
[12] K. Kim, Y. Park, *Nat. Commun.* **2017**, *8*, 15340.
[13] A. Kuś, M. Dudek, B. Kemper, M. Kujawińska, A. Vollmer, *J. Biomed. Opt.* **2014**, *19*, 046009.
[14] B. Simon, M. Debailleul, M. Houkal, C. Ecoffet, J. Bailleul, J. Lambert, A. Spangenberg, H. Liu, O. Soppera, O. Haeberlé, *Optica* **2017**, *4*, 460.
[15] C. Zuo, J. Sun, J. Li, A. Asundi, Q. Chen, *Opt. Lasers Eng.* **2020**, *128*, 106003.
[16] R. Horstmeyer, J. Chung, X. Ou, G. Zheng, C. Yang, *Optica* **2016**, *3*, 827.
[17] N. Zhou, J. Li, J. Sun, R. Zhang, Z. Bai, S. Zhou, Q. Chen, C. Zuo, *Opt. Lett.* **2022**, *47*, 969.
[18] J. Sun, C. Zuo, J. Zhang, Y. Fan, Q. Chen, *Sci. Rep.* **2018**, *8*, 7669.
[19] J. Li, N. Zhou, J. Sun, S. Zhou, Z. Bai, L. Lu, Q. Chen, C. Zuo, *Light: Sci. Appl.* **2022**, *11*, 154.
[20] S. Zhou, J. Li, J. Sun, N. Zhou, H. Ullah, Z. Bai, Q. Chen, C. Zuo, *Optica* **2022**, *9*, 1362.
[21] C. Zuo, J. Li, J. Sun, Y. Fan, J. Zhang, L. Lu, R. Zhang, B. Wang, L. Huang, Q. Chen, *Opt. Lasers Eng.* **2020**, *135*, 106187.
[22] S. Zhou, J. Li, J. Sun, N. Zhou, Q. Chen, C. Zuo, *J. Biophotonics* **2022**, *15*, 202100272.
[23] M. F. Juette, T. J. Gould, M. D. Lessard, M. J. Mlodzianoski, B. S. Nagpure, B. T. Bennett, S. T. Hess, J. Bewersdorf, *Nat. Methods* **2008**, *5*, 527.
[24] A. Descloux, K. Grußmayer, E. Bostan, T. Lukes, A. Bouwens, A. Sharipov, S. Geissbuehler, A.-L. Mahul-Mellier, H. Lashuel, M. Leutenegger, T. Lasser, *Nat. Photonics* **2018**, *12*, 165.
[25] R. Zhang, N. Zhou, H. Tang, M. Xia, Z. Cai, J. Sun, Q. Chen, C. Zuo, *Laser Photonics Rev.* **2024**, *18*, 2300770.
[26] P. Gao, B. Yao, I. Harder, J. Min, R. Guo, J. Zheng, T. Ye, *JOSA A* **2011**, *28*, 434.
[27] P. Gao, B. Yao, J. Min, R. Guo, J. Zheng, T. Ye, I. Harder, V. Nercissian, K. Mantel, *Opt. Express* **2011**, *19*, 1930.
[28] C. Zuo, Q. Chen, W. Qu, A. Asundi, *Opt. Lett.* **2013**, *38*, 3538.
[29] C. Falldorf, M. Agour, C. v. Kopylow, R. B. Bergmann, *Appl. Opt.* **2010**, *49*, 1826.
[30] P. F. Almoro, L. Waller, M. Agour, C. Falldorf, G. Pedrini, W. Osten, S. G. Hanson, *Opt. Lett.* **2012**, *37*, 2088.
[31] J. M. Soto, J. A. Rodrigo, T. Alieva, *Opt. Express* **2017**, *25*, 15699.
[32] M. H. Jenkins, T. K. Gaylord, *Appl. Opt.* **2015**, *54*, 8566.
[33] P. Sarder, A. Nehorai, *IEEE Signal Process. Mag.* **2006**, *23*, 32.
[34] R. Ling, W. Tahir, H.-Y. Lin, H. Lee, L. Tian, *Biomed. Opt. Express* **2018**, *9*, 2130.
[35] A. Matlock, L. Tian, *Biomed. Opt. Express* **2019**, *10*, 6432.
[36] L. Tian, L. Waller, *Opt. Express* **2015**, *23*, 11394.
[37] Z. Bai, Q. Chen, H. Ullah, L. Lu, N. Zhou, S. Zhou, J. Li, C. Zuo, *Opt. Lasers Eng.* **2022**, *156*, 107082.
[38] J. Brown, S. Beer, in *Quantum Technology: Driving Commercialisation of an Enabling Science III*, vol. *12335*, SPIE, Bellingham **2023**, pp. 43–47.
[39] J. Zhu, H. Wang, L. Tian, *Opt. Express* **2022**, *30*, 32808.
[40] M. Chen, D. Ren, H.-Y. Liu, S. Chowdhury, L. Waller, *Optica* **2020**, *7*, 394.
[41] J. Lim, K. Lee, K. H. Jin, S. Shin, S. Lee, Y. Park, J. C. Ye, *Opt. Express* **2015**, *23*, 16933.
[42] N. Zhou, J. Sun, R. Zhang, R. Ye, J. Li, Z. Bai, S. Zhou, Q. Chen, C. Zuo, *ACS Photonics* **2023**, *10*, 2461.
[43] Z. Zhang, L. Bai, L. Cong, P. Yu, T. Zhang, W. Shi, F. Li, J. Du, K. Wang, *Nat. Biotechnol.* **2021**, *39*, 74.
[44] L. Schermelleh, P. M. Carlton, S. Haase, L. Shao, L. Winoto, P. Kner, B. Burke, M. C. Cardoso, D. A. Agard, M. G. Gustafsson, H. Leonhardt, J. W. Sedat, *Science* **2008**, *320*, 1332.
[45] J. Qian, Y. Cao, Y. Bi, H. Wu, Y. Liu, Q. Chen, C. Zuo, *eLight* **2023**, *3*, 4.
[46] D. Dong, X. Huang, L. Li, H. Mao, Y. Mo, G. Zhang, Z. Zhang, J. Shen, W. Liu, Z. Wu, G. Liu, Y. Liu, H. Yang, Q. Gong, K. Shi, L. Chen, *Light: Sci. Appl.* **2020**, *9*, 11.


© 2024 Wiley-VCH GmbH

18638899, 0, Downloaded from https://onlinelibrary.wiley.com/doi/10.1002/lpor.202400387 by Nanjing University Of Science, Wiley Online Library on [01/07/2024]. See the Terms and Conditions (https://onlinelibrary.wiley.com/terms-and-conditions) on Wiley Online Library for rules of use; OA articles are governed by the applicable Creative Commons License